

A Novel Axial Flux Eddy Current Sensor with Perpendicular Coils for Speed Measurement

Mehran Mirzaei, Pavel Ripka, Vaclav Grim, and Zdenek Hazdra

Abstract— There is an increasing demand to use high-efficiency and high power density electrical machines in the automotive industry for transportation electrification. Induction motors are a cost-effective option for traction applications that need contactless, precise, and compact speed sensors. This paper presents an axial flux eddy current sensor with a compact and simple structure for measuring the rotating speed of iron shafts. It presents a novel configuration of the coils, which are positioned perpendicularly to each other. The sensor consists of two D-shaped excitation coils and two D-shaped pick-up coils in a double layer structure. The coils are shielded by a disc-shaped magnetic core or shield. Two iron shafts with different material properties are considered. A new cup-shape configuration of nonmagnetic copper and aluminum caps mounted on iron shafts is used to improve sensitivity and suppress susceptibility to shaft material parameters and airgap variation. 2D and 3D finite element methods are utilized for a performance analysis of the sensor. The measurements are performed at various speeds up to ± 3000 rpm and at different excitation frequencies from 400 Hz to 4 kHz. The eddy current speed sensor has excellent linearity characteristics with nonlinearity error 0.15 %. The geometry was optimized for maximum sensitivity. The fault tolerant capability of the sensor is also evaluated.

Index Terms— Analysis, axial flux, eddy current sensor, speed measurement, perpendicular coils

I. INTRODUCTION

SPEED measurements are essential for the control, maintenance and protection of moving devices for various applications, for example, high-speed railways [1] and vehicles. An important contribution to the solution to the fast temperature rise of the earth is the acceleration of transportation electrification. Permanent magnet (PM) motors with a radial flux structure using an interior PM rotor and an axial flux structure with a surface-mounted PM rotor are the most commonly used machines for electrified transportation. Nonetheless, they suffer from a critical drawback when using expensive rare earth magnets with high coercive force. These magnets have a high risk of demagnetization under overload and overheating conditions and require sophisticated and complicated rotor cooling. Industrial and commercial induction motors are widely used in various power and speed ranges for electrical transportation [2]-[6], for example, traction motors of electrical vehicles. Speed measurement of rotating shafts of

induction machines with the use of cost-effective and robust sensors and methodologies is therefore in great demand. Axial airgap induction machines have high power density because of their short axial length [7]-[10], which is a crucial advantage for the electrical vehicles demanding compact and low weight electrical machines. The increasing power density of electrical machines makes less extra room available in the non-drive end shaft region, and compact speed sensors are therefore essential.

A sensorless speed estimation method is a nondestructive approach, and unlike physical sensors it can be installed without requiring machines to be overhauled [11]-[12]. It requires complicated hardware for signal processing, and could therefore, be less cost-effective and slower. In addition, the method is not fault tolerant to electrical failures in stator and rotor circuits. A stationary magnetic encoder installed on the stator of a permanent magnet flux switching machine was presented in [13]. It requires complicated post processing of the signals of the Hall sensors that are used, and it is prone to overheating in the stator. A similar methodology is used in [14]-[15] using stationary Hall sensors installed in the stator slot openings of an induction machine a switched reluctance machine. The methodology faces the same disadvantages as in [13]. A self-powered flexible sensor based on a triboelectric nanogenerator was used for speed measurement at very low speeds [16]. It is prone to dust and dirt due its electrostatic-based operation.

Tachometers are utilized for speed measurements for rotating shafts [17]-[18], which have a non-complicated structure. They are not contactless, and their rotating part needs to be mounted on a rotating shaft. Optical encoders using moving optical gear for speed measurements have high reliability, accuracy, and resolution, together with a compact size [19]. The optical encoders have a lower weight and rotational inertia than tachometers, and they are well-suited for applications with high acceleration and deceleration rates. They are prone to the effects of dirt, oil, and dust. Unlike optical encoders, resolvers based on variable reluctance operation [20] are more durable than optical encoders. They are suitable for applications in a harsh environment and in the presence of high vibrations and temperatures [21]. The resolvers are more expensive and less precise than optical encoders. They lose accuracy when a rapid speed change occurs. The moving magnetic gear of resolvers has to be connected to the rotating shaft, as in the case of optical encoders and tachometers.

Installing a moving part on the rotating shaft for position and

The final version of his paper was published at Sensors and Actuators 365 (2024), 114917, <https://doi.org/10.1016/j.sna.2023.114917>

speed measurement in the standard optical encoders, tachometers, and resolvers makes them vulnerable in high vibration applications [22], for example, compact traction motors. A new optical encoder was presented in [22] using black non-reflective and white reflective marks installed on the rotating shaft. Encapsulation against dust and dirt is needed for optical and infrared-based measurement, which is not practically feasible for highly vibrating rotating machinery used in transportation vehicles. Using contactless and compact speed sensors with a cost-effective and simple structure is necessary for traction motors with both direct-drive in-wheel and indirect-drive using gearbox structures.

The induced eddy current in the solid conductive smooth-surface objects is utilized in various applications; for example, eddy current brakes [23]-[24] use the motional component of the induced eddy current. The motional component of induced eddy current is generated by relative motion between excitation coils and conductive moving objects. The motional component of the induced eddy current in moving conductive substances with a smooth surface could be utilized for measuring the speed of moving fluids and solid objects. The earliest usage of eddy current for speed measurement was reported as a flowmeter [25]. An electromagnetic flowmeter with non-contact electrodes was presented in [26]. It utilizes the induced voltage caused by the speed effect of a moving fluid in applied magnetic fields. An alternative approach was presented in [27] using contactless toroidal coils. An eddy current speed sensor utilizing the forces caused by the motional component of the induced eddy current in a conductive sheet developed in [28] has a complicated mechanical structure. Eddy current sensors for linear speed measurements of moving plates were presented using one excitation coil and two pick-up coils in [29] and two perpendicular coils in [30] with circular forms. Later, a speed sensor for linear speed measurement of a moving rod was presented in [31], based on the same coils arrangements as in [27] and [29]. An eddy current speed sensor was presented in [32] using the fluxgate effect in an amorphous ring core to measure the field of eddy currents. This rather complicated sensor has a poor linearity error of approximately 5%. An eddy current speed sensor using a Hall sensor with permanent magnet excitation was presented in [33], which shows poor offset stability. The same configuration of an eddy current speed sensor with Hall sensors and permanent magnet excitation as in [33] was developed in [34]. Using magnet excitation makes the speed sensor vulnerable to external low frequency and DC fields. Only aluminum material was used in [29]-[34] for the conductive moving part. A linear eddy current speed sensor with two perpendicular coils was presented in [35] for speed measurement of solid iron plates. Rotational eddy current speed sensors with cylindrical and axial flux configurations were described in [36]-[38].

A novel compact eddy current speed sensor with an axial flux configuration is presented in this paper. It has a short axial length of 6.5 mm. The sensor has two excitation coils and two pick-up coils, which are located perpendicularly. In our earlier research we already found that the cylindrical speed sensor with perpendicular configuration of the coils [38] shows higher sensitivity than the conventional cylindrical configuration with

an excitation coil and two antiseriably connected pick-up coils [36]. In this paper we use this principle for improvement of axial speed sensor. The sensitivity of the proposed sensor was improved by 150% in comparison with the authors' earlier constructed sensor with an axial flux structure [37]. Another novelty described in this paper are non-magnetic caps at the end of the shaft. We show the advantages of caps compared to simple conductive disks used in [37]. The finite element method (FEM) is used for modeling and for a performance assessment of the sensor. The experiments are performed at various excitation frequencies and speeds.

II. STRUCTURE AND OPERATION THEORY OF THE SENSOR

The 3D configuration of the eddy current speed sensor is shown in Fig. 1, which is the structure of the sensor prototype. It includes two excitation coils and two pick-up coils, and a magnetic shield. The disc-shaped shield is a silicon steel lamination 30 mm in diameter and 0.5 mm in thickness. Its conductivity was measured at 3.41 MS/m, and its initial relative magnetic permeability was estimated as 1000 [37]. Two excitation coils and two pick-up coils could be connected in series or in parallel. Each excitation coil and pick-up coil has 500 turns with axial height $h_w = 2.5$ mm and radial thickness $t_w = 2$ mm (Fig. 1). The distance between the coils and the disc shield is 1 mm. Two solid iron shafts 30 mm in diameter are used for the modeling and the experiments:

- 1- Iron-a with conductivity 5.24 MS/m
- 2- Iron-b with conductivity 4.51 MS/m.

Fig. 2 shows the schematic view of the eddy current distributions on the end surface of the solid iron shaft at zero and nonzero rotating speeds. The rotating speed causes the motional component of the induced eddy current, which causes the distribution of the eddy currents to be asymmetric. The asymmetric distribution of the eddy current causes asymmetric magnetic flux distribution, as shown in Fig. 3 with a vector plot. The voltage is zero in the pick-up coils with symmetric magnetic flux distribution at zero speed. The voltage is induced with an asymmetric magnetic flux distribution at nonzero speed and AC excitation. The induced voltage is proportional to the rotating speed of the shaft, which can be utilized as a speed meter.

III. THEORETICAL ANALYSIS

The governing Maxwell equations are as follows [29]:

$$\begin{aligned} \nabla \cdot B &= 0, & B &= \mu H, & \nabla \times H &= J \\ \nabla \times E &= -\sigma \frac{\partial B}{\partial t} \\ J &= \sigma E + \sigma v \times B, & v &= r \cdot 2\pi \frac{n_r}{60} \end{aligned} \quad (1)$$

where, B , E , H , and J are the magnetic flux density, the electric field intensity, the magnetic field strength, the current density, respectively. σ , μ , and v are the conductivity, the magnetic permeability, and the linear speed in m/s, respectively. r is the radius and n_r is the rotating speed of the shaft in rpm.

The final version of his paper was published at
Sensors and Actuators 365 (2024), 114917, <https://doi.org/10.1016/j.sna.2023.114917>

The induced eddy current $J = J_t + J_m$ in the conductive rotating shaft has two components according to (1): J_t is the transformer component and J_m is the motional component.

$$(2) \quad J_t = \sigma E, \quad J_m = \sigma v \times B$$

The induced voltages $U_{p,1}$ and $U_{p,2}$ in the two pick-up coils are equal, $U_{p,1} = U_{p,2}$. The resultant voltage U_p is equal to $U_{p,1} + U_{p,2} = 2 \cdot U_{p,1}$ when the two pick-up coils are in series.

2D and 3D time stepping FEM are used for the theoretical analysis. 3D FEM is more precise for eddy current analysis as the axial flux speed sensor is a 3D electromagnetic device. 2D FEM is preferred for fast parametric analysis of the performance of the eddy current sensor. Maxwell/Ansys software is used for the 2D and 3D FEM analyses. The sliding mesh method is utilized to model the rotating shaft motion in 2D and 3D. Equation (3) is extracted from the Maxwell equations in (1) for FEM analysis [39].

$$(3) \quad \begin{aligned} \nabla \cdot B &= 0 \rightarrow B = \nabla \times A \\ \nabla \times \left(\frac{1}{\mu} \nabla \times A \right) &= J_s - \sigma \frac{\partial A}{\partial t} - \sigma \cdot \nabla V + \sigma \cdot v \times (\nabla \times A) \end{aligned}$$

where, A and V are magnetic vector potential and electric scalar potential, respectively. J_s is the source current density.

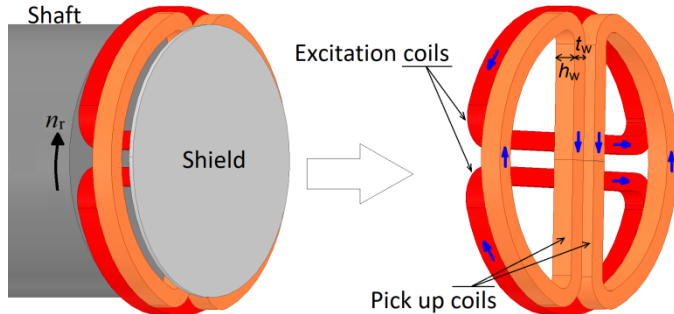


Fig. 1. Model of the eddy current speed sensor with the shaft rotating at speed n_r .

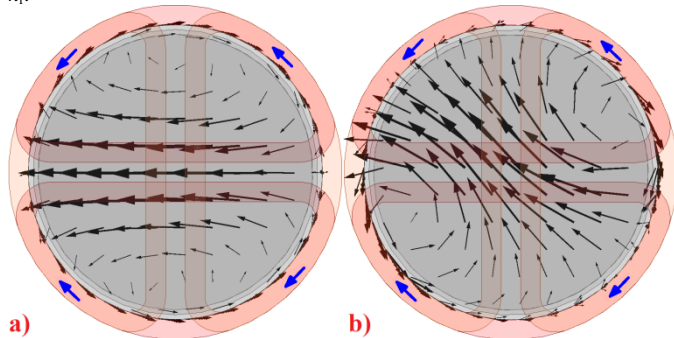


Fig. 2. Eddy current distribution on the surface of the end part of the shaft – a) symmetric at zero speed, b) asymmetric at nonzero speed.

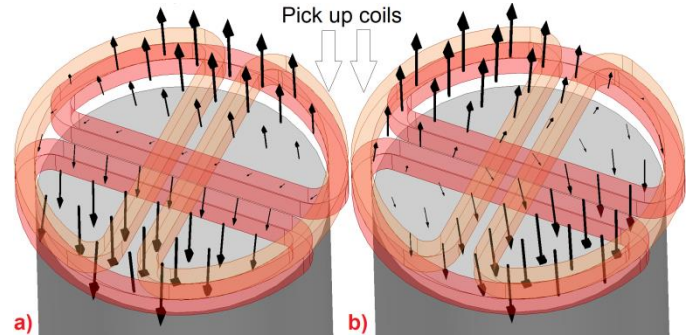


Fig. 3. Vector plot of the link of the magnetic fields to the pick-up coils – a) symmetric at zero speed, b) asymmetric at nonzero speed.

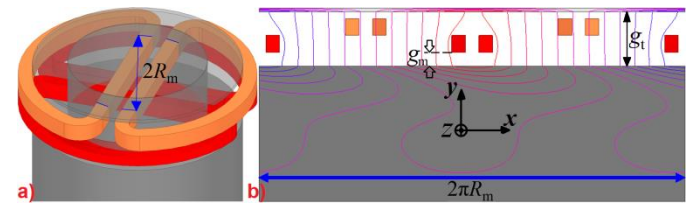


Fig. 4. a) 3D model of axial flux eddy current speed sensor, b) linearized 2D model in y - x plane – g_m is the magnetic and mechanical gap between coils and rotating part and g_t is the distance between magnetic shield and rotating part

A. 2D FEM

A linearized approximate model for 2D analysis is developed, as shown in Fig. 4. In order to generate a 2D model of the 3D axial flux structure, a slice with a mean radius, R_m , from the 3D model in Fig. 4 a) is flattened as shown in Fig. 4 b). It is convenient for the analysis of axial flux magnetic devices to flatten or roll out their 3D configuration for analysis simplification using a 2D model [40]-[41]. Equation (3) is converted to (4) for 2D analysis. A_z is the z -component of the magnetic vector potential [24].

$$(4) \quad -\frac{1}{\mu} \nabla^2 A_z = J_{s,z} - \sigma \frac{\partial A_z}{\partial t} - \sigma \cdot v \cdot \frac{\partial A_z}{\partial x}$$

The conductivity and the relative magnetic permeability are considered $\sigma = 5.24$ MS/m and $\mu_r = 100$, respectively. The mean radius, R_m , is selected as 10 mm. Therefore, the longitudinal length of the 2D model is $2\pi R_m = 62.8$ mm. The magnetic gap g_m is the axial distance between the rotating shaft and the coils, which is initially considered to be 2 mm. The voltage increases and the flux linkage decreases with increasing frequency up to 4 kHz, as shown in Fig. 5. Therefore, the voltage or the sensitivity of the sensor is higher at higher frequencies up to 4 kHz, despite the reduced flux linkage at higher frequencies. The voltage is proportional to the flux linkage multiplied by the frequency. Therefore, for example, increasing the frequency 40-times from 100 Hz to 4 kHz reduces the flux linkage by more than 93% and increases the induced voltage about 2.75-times.

The voltage and the voltage gradient to gap gradient ratio decrease with the increasing magnetic gap (Fig. 6). This shows that the eddy current sensor is less susceptible to the change in the magnetic gap, g_m for larger gaps, despite its lower

The final version of his paper was published at Sensors and Actuators 365 (2024), 114917, <https://doi.org/10.1016/j.sna.2023.114917>

sensitivity. For example, increasing the gap from 0.75 mm to 3.5 mm (466.7 %) reduces the sensitivity of the sensor only by 50%. Nevertheless, the susceptibility of the sensor to a change in the gap decreases by more than 50%. Selecting the magnetic gap, $g_m = 2$ mm is a compromise between the maximum sensitivity of the sensor and its minimum susceptibility to the variation of g_m . A larger value of g_m is helpful for the mechanical installation of the sensor. Nonetheless, decreasing g_m to a lower value is practically feasible, as shown for 1.0 mm in [37].

Fig. 7 a) presents the voltage-to-current ratio versus speed up to 3000 rpm. It shows high linearity versus speed, which theoretically shows the suitability of the sensor for the rotating speed measurement with a maximum nonlinearity error of 0.05%. The total voltage of series connected pickup coils, $U_{p,1} + U_{p,2}$ is double of each pickup coil voltage, $U_{p,1} = U_{p,2}$ as shown in Fig. 7 a) and Fig. 7 b).

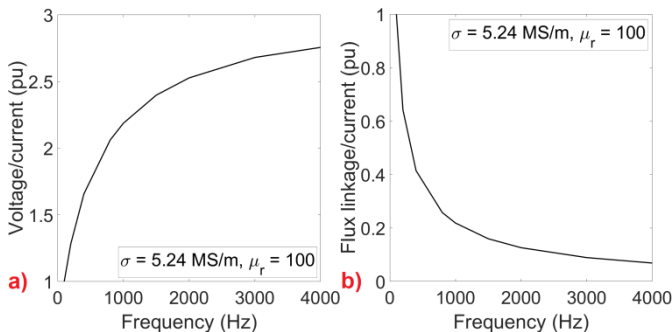


Fig. 5. a) The induced voltage to excitation current ratio versus frequency, b) the flux linkage to the current ratio versus frequency (2D FEM) – for $g_m = 2.0$ mm and 3000 rpm

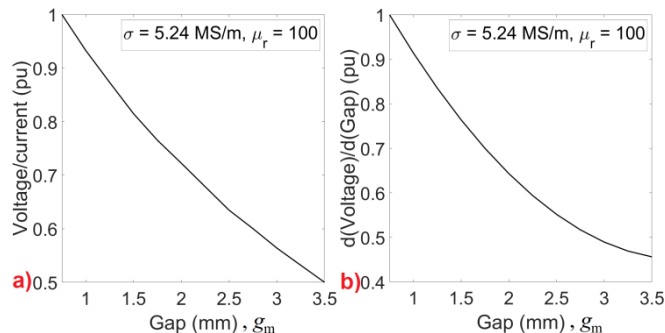


Fig. 6. A) The voltage to current ratio versus the magnetic gap, g_m , b) The gradient of the voltage to the gradient of the magnetic gap, g_m ratio versus the magnetic gap (2D FEM) -for 1000 Hz and 3000 rpm

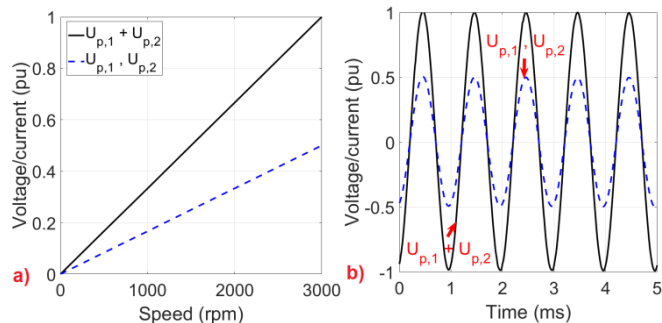


Fig. 7. a) The voltage to current ratio versus speed , b) The voltage to current ratio versus time at 3000 rpm (2D FEM) - 1000 Hz ($\sigma = 5.24$ MS/m and $\mu_r = 100$)

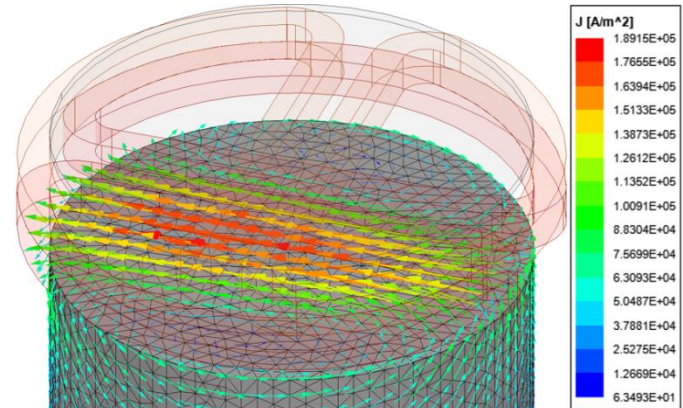


Fig. 8. Eddy current distribution on the surface of a solid iron rotating shaft at 1000 Hz, 3000 rpm, $I = 10$ mA – 3D FEM

B. 3D FEM

The performance of the eddy current speed sensor is also analyzed using 3D FEM to evaluate the effects of the iron shaft material on the performance of the speed sensor. Fig. 8 shows the eddy current distribution on the surface of the end part of the shaft. Table I presents the sensor voltage U_p to current I , for materials Iron-a and Iron-b with relative magnetic permeabilities $\mu_r = 50, 100, 150$ at 3000 rpm. Increasing the conductivity from 4.51 MS/m to 5.24 MS/m (16% change) increases the sensitivity of the sensor by 4.5%. Increasing μ_r from 50 to 150 reduces the sensor voltage by 31% at 400 Hz excitation frequency and by 25% at 1000 Hz.

TABLE I
CALCULATED VOLTAGE TO APPLIED CURRENT, IRON SHAFT – 3D FEM

$U_p / I, \text{ mV/A } (I = 10 \text{ mA}) - 3000 \text{ rpm}$		400 Hz	1000 Hz
Iron-a	$\mu_r = 50$	181	258
	$\mu_r = 100$	143	218
	$\mu_r = 150$	125	193
Iron-b	$\mu_r = 50$	172	248
	$\mu_r = 100$	137	209
	$\mu_r = 150$	118	185

IV. MEASUREMENTS

The measurement set-up and the elements of the eddy current speed sensor are shown in Fig. 9 and Fig. 10. Serial connection of the excitation and pick-up coils is considered for the eddy current speed sensor experiment. The excitation coils with total resistance of 523 Ω are connected to the signal generator with 10 V voltage amplitude and 50 Ω internal resistance, through the external resistor $R = 99.3 \Omega$. A TLE5012 absolute angle sensor from Infineon Technologies is used to measure the reference speed [37]. This sensor is based on the giant magnetoresistive (GMR) effect. It has a resolution of 0.01° with a maximum 1.0° angular error. The magnetic field of a mounted permanent magnet on the non-drive end shaft of the prime mover in Fig. 9 is used for the excitation of the angular sensor.

The speed sensor voltage is measured by an SR830 DSP lock-in amplifier with a 16-bit Analog-to-Digital Converter, which

The final version of his paper was published at Sensors and Actuators 365 (2024), 114917, <https://doi.org/10.1016/j.sna.2023.114917>

is connected to the pick-up coils as shown in Fig. 11. The voltage drop across the external resistance, which is proportional to the current of the excitation coils, is used as a reference signal for the lock-in amplifier. The measured voltage using the lock-in amplifier has real and imaginary components. The real component of the measured voltage is in phase with the excitation current, and the imaginary component is in quadrature. The measured currents for various excitation frequencies are presented in Table II.

The measurements are performed at excitation frequencies $f = 400$ Hz, 1000 Hz, and 4000 Hz for a speed range of ± 3000 rpm with a speed step of 300 rpm.



Fig. 9. Experimental setup of the eddy current speed sensor



Fig. 10. Experiment elements: iron shafts, sensor coils and aluminum and copper caps.

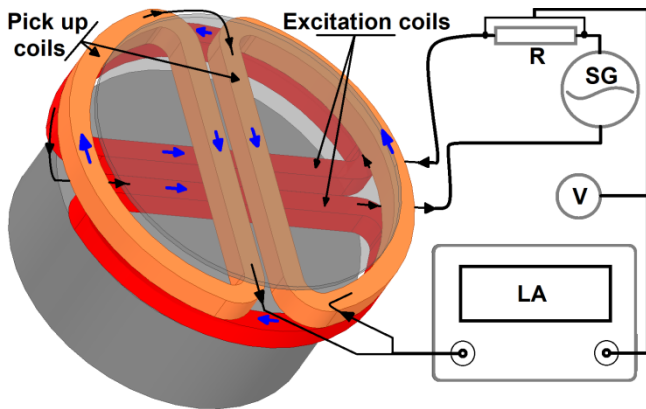


Fig. 11. Schematic model of measurement elements used for eddy current speed sensor: Lock-in amplifier (LA), signal generator (SG), external resistance (R) and voltmeter (V).

I (mA)	400 Hz	1000 Hz	4000 Hz
Iron-a	10.4	10.1	7.5
Iron-b	10.4	10.1	7.4
Iron-a+Al cap	10.4	10.2	8.5
Iron-a+Copper cap	10.4	10.2	8.6

	10.3	10.1	8.5
Iron-b+Al cap	10.3	10.2	8.6

A. Only Iron Shaft

The measured real $U_{p,r}$ and imaginary $U_{p,i}$ components of the output voltage to the excitation current ratio versus speed are presented in Fig. 12 and Fig. 13 for solid iron shafts with materials Iron-a and Iron-b. Both the real and the imaginary components of the voltage have high linearity, which shows the suitability of the sensor for speed measurements.

Table III and table IV present the sensitivity coefficients of the sensor:

$$K_r = \frac{U_{p,r}}{n_r \cdot I}, \quad K_i = \frac{U_{p,i}}{n_r \cdot I}$$

$$K_a = \frac{U_{p,a}}{n_r \cdot I}, \quad U_{p,a} = \sqrt{U_{p,r}^2 + U_{p,i}^2}$$

(5)

where, K_r corresponds to the real component of the voltage $U_{p,r}$, K_i corresponds to the imaginary component of the voltage. The sensitivity coefficient corresponding to the absolute value of the voltage, K_a is also presented in Table V.

The sensor sensitivity corresponding to $U_{p,a}$ decreases by 6.8% to 7.8% when the shaft material changes from Iron-a to Iron-b, which has 14% lower conductivity. The real component of the voltage is less vulnerable than the imaginary component to changes in the material properties. The sensitivity of the sensor increases with frequency for the absolute value of the voltage.

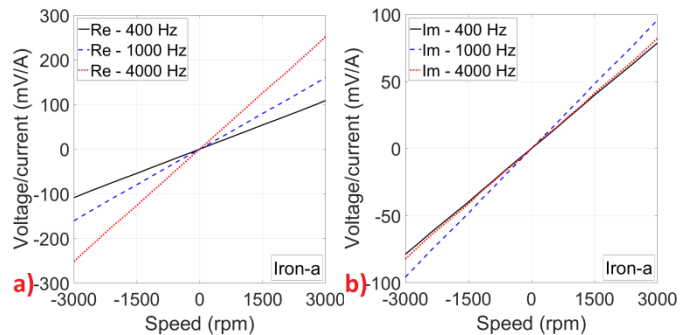


Fig. 12. The voltage-to-current ratio versus speed for Iron-a, a) real component (Re), b) imaginary component (Im) – measurement

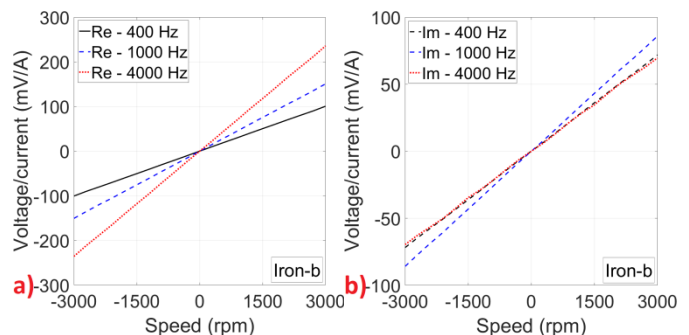


Fig. 13. The voltage-to-current ratio versus speed for Iron-b, a) real component (Re), b) imaginary component (Im) – measurement

TABLE III
SENSITIVITY COEFFICIENTS OF THE SENSOR – REAL COMPONENT

The final version of his paper was published at
Sensors and Actuators 365 (2024), 114917, <https://doi.org/10.1016/j.sna.2023.114917>

$K_r, \mu V/(rpm \cdot A)$	400 Hz	1000 Hz	4000 Hz
Iron-a	36.1	53.2	83.7
Iron-b	33.5	50.2	78.5
Iron-a+Al cap	165.1	82.1	40.9
Iron-a+Copper cap	82.5	54.3	33.1
Iron-b+Al cap	161.0	80.0	40.7
Iron-b+Copper cap	86.2	57.0	34.9

TABLE IV
SENSITIVITY COEFFICIENTS OF THE SENSOR – IMAGINARY COMPONENT

$K_i, \mu V/(rpm \cdot A)$	400 Hz	1000 Hz	4000 Hz
Iron-a	26.3	31.9	27.3
Iron-b	24.0	28.7	23.4
Iron-a+Al cap	-10.0	-65.7	-24.6
Iron-a+Copper cap	-47.3	-25.6	-24.6
Iron-b+Al cap	-10.2	-64.7	-25.4
Iron-b+Copper cap	-49.6	-26.6	-25.3

TABLE V
SENSITIVITY COEFFICIENTS OF THE SENSOR – ABSOLUTE VALUE

$K_a, \mu V/(rpm \cdot A)$	400 Hz	1000 Hz	4000 Hz
Iron-a	44.7	62.0	88.0
Iron-b	41.2	57.8	81.9
Iron-a+Al cap	165.4	105.2	47.7
Iron-a+Copper cap	95.1	60.0	41.2
Iron-b+Al cap	161.3	102.9	48.0
Iron-b+Copper cap	99.5	62.9	43.1

B. Iron Shaft with a Nonmagnetic Cap

Adding a nonmagnetic cap on the iron shafts, as shown in Fig. 14, significantly enhances the performance of the sensor. The height h_c , the thickness t_c , and the inner and outer diameters D_{ci} and D_{co} of the aluminum cap are 11.4 mm, 3.15 mm, 30 mm and 32.2 mm, respectively. These dimensions are 11.7 mm, 4.3 mm, 30 mm and 33.7 mm for a copper cap. Fig. 15 - Fig. 18 show the measured real and imaginary components of the sensor voltage-to-current ratio versus speed for iron shafts (Iron-a and Iron-b) with aluminum and copper caps. The conductivities of aluminum and copper caps have been measured 21.0 MS/m and 56.6 MS/m, respectively.

The sensitivity coefficient of the sensor corresponding to the absolute value of voltage $U_{p,a}$ in Table V changes by between 0.6% and 2.5% for the shafts with an aluminum cap when the shaft material changes from Iron-a to Iron-b. The change is about 4.6% for the shafts with a copper cap. This shows that the sensor is less susceptible to the material properties of the iron shaft when a nonmagnetic cap is used.

The sensitivity of the sensor using a nonmagnetic cap is greater than with only an iron shaft at lower frequencies, as the magnetic flux penetration and the skin depth, $\delta = 1/(\pi f \mu_0 \mu_r \sigma)^{0.5}$, in the nonmagnetic cap are higher at lower frequencies. The same phenomena also occur for an aluminum cap in comparison with a copper cap, due to the lower conductivity of the aluminum cap and its greater skin depth. Reducing the thickness of the cap t_c could improve the sensitivity enhancement at higher frequencies.

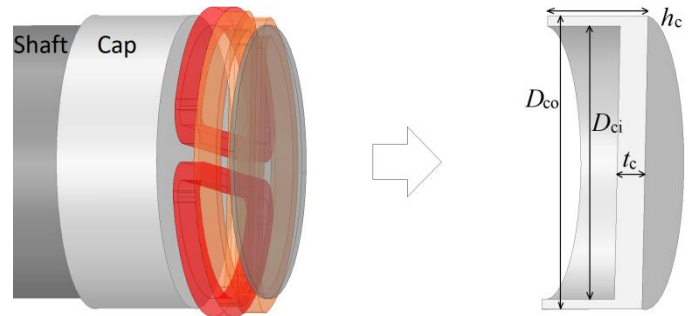


Fig. 14. Model of the eddy current speed sensor with a nonmagnetic cap

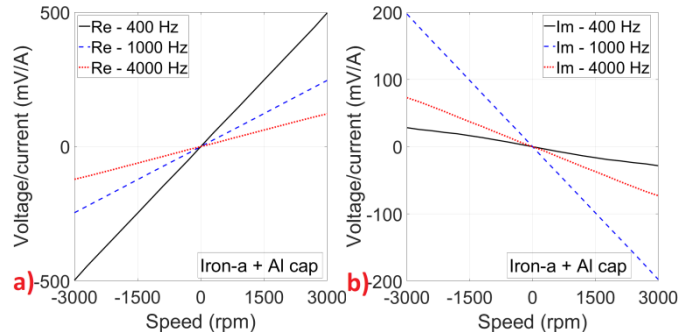


Fig. 15. The voltage-to-current ratio versus speed for Iron-a with an aluminum cap, a) real component (Re), b) imaginary component (Im) – measurement

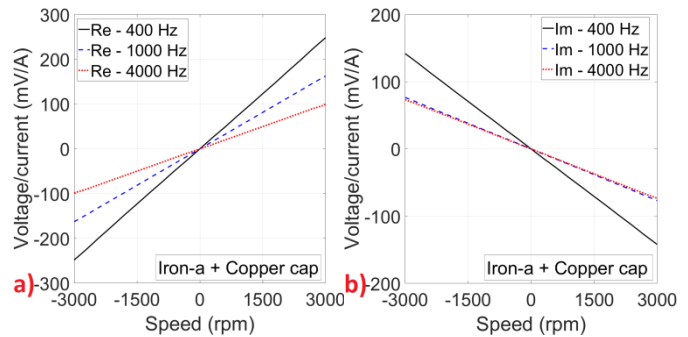


Fig. 16. The voltage-to-current ratio versus speed for Iron-a with a copper cap, a) real component (Re), b) imaginary component (Im) – measurement

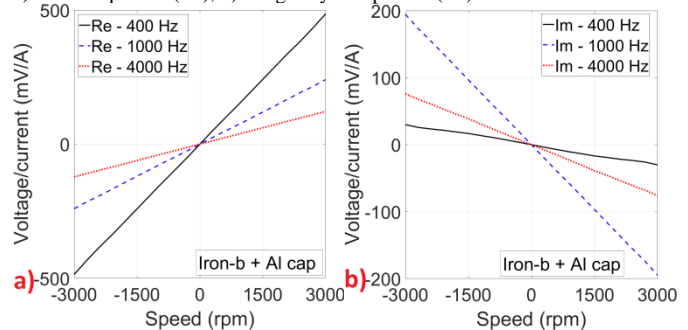


Fig. 17. The voltage-to-current ratio versus speed for Iron-b with an aluminum cap, a) real component (Re), b) imaginary component (Im) – measurement

The final version of his paper was published at

Sensors and Actuators 365 (2024), 114917, <https://doi.org/10.1016/j.sna.2023.114917>

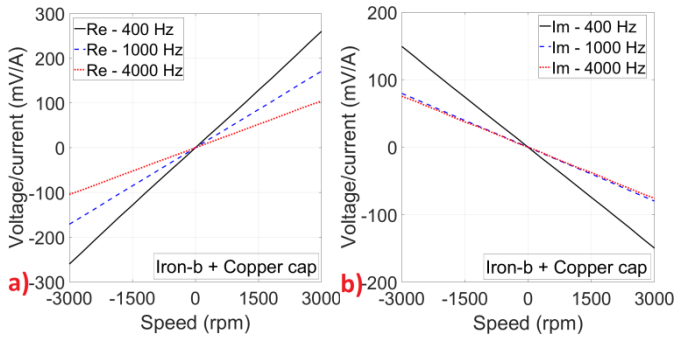


Fig. 18. The voltage-to-current ratio versus speed for Iron-b with a copper cap, a) real component (Re), b) imaginary component (Im) – measurement

Table VI presents the flux linkage coefficients $C_a = K_a/(2\pi f)$ at frequencies of $f = 400$ Hz, 1000 Hz and 4000 Hz, which decrease with increasing frequency. This shows experimentally that the sensor is more sensitive to the rotating shaft speed at lower frequencies in terms of the flux linkage value. However, the sensor voltage is higher at higher frequencies up to 4000 Hz, as the sensor voltage is proportional to the flux linkage multiplied by the frequency.

C_a , nWb/(rpm·A)	400 Hz	1000 Hz	4000 Hz
Iron-a	17.8	9.9	3.5
Iron-b	16.4	9.2	3.3
Iron-a+Al cap	65.8	16.7	1.9
Iron-a+Copper cap	37.8	9.5	1.6
Iron-b+Al cap	64.2	16.4	1.9
Iron-b+Copper cap	39.6	10	1.7

A 3D FEM analysis of an eddy current speed sensor with an aluminum cap and with a copper cap was performed at 400 Hz and at 1000 Hz and is presented in Table VII and Table VIII for the absolute value of the voltage. Various $\mu_r = 50, 100$ and 150 are considered. The sensor voltages change only between 0.4% and 7.3% when μ_r increases by 200% from 50 to 150.

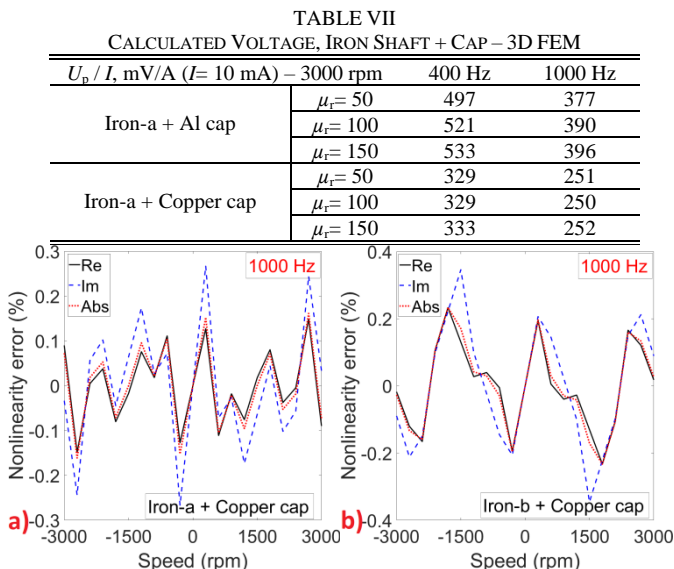


Fig. 19. The nonlinearity error versus speed for Iron-a and Iron-b with a copper cap, a) real component (Re), b) imaginary component (Im) – measurement

U_p / I , mV/A ($I = 10$ mA) – 3000 rpm	400 Hz	1000 Hz	
Iron-b + Al cap	$\mu_r = 50$	503	381
	$\mu_r = 100$	526	393
	$\mu_r = 150$	537	399
Iron-b + Copper cap	$\mu_r = 50$	330	251
	$\mu_r = 100$	332	250
	$\mu_r = 150$	334	252

Precise 3D FEM modeling can be further used to optimize the design of the sensor. For example, the calculated voltage with an aluminum cap in Tables VII and VIII using 3D FEM matches well with experiments in Fig. 15 and Fig. 17 with 4.2% error, which shows that the accuracy of 3D FEM is appropriate.

C. Nonlinearity Error Analysis

The nonlinearity error of the eddy current sensor is calculated on the basis of the deviation of the actual measured values from a best fitted straight line, ΔU_p . For example, it can be described as a fraction of full scale $U_{p,max}$ as a percentage (%): $\Delta U_p / U_{p,max} \cdot 100\%$. Fig. 19 shows the nonlinearity error of the speed sensor for an iron shaft with a copper cap, which can be as low as 0.15%.

V. OPTIMIZATION

Table IX presents the calculated voltage to current ratio using 3D FEM versus cap thickness. The sensitivity of the sensor is evaluated with decreasing cap thickness t_c (see Fig. 14) for an excitation frequency of 1000 Hz. Table IX shows that the sensor voltage for an aluminum cap increases by 97% with the optimum thickness of $t_c = 0.5$ mm in comparison with the sensor voltage using the original value of thickness, $t_c = 3.15$ mm in Table VII. And it increases for a copper cap by 223% with the optimum thickness $t_c = 0.25$ mm in Table IX mm in comparison with the sensor voltage using original value of thickness, $t_c = 4.3$ mm in Table VII. The magnetic flux penetration and the skin depths, $\delta = 1/(\pi f \mu_0 \mu_r \sigma)^{0.5}$ are calculated 3.47 mm for aluminum and 2.12 mm for copper. A higher skin depth to cap thickness ratio helps to increase the magnetic penetration depth and, therefore, the sensitivity of the eddy current speed sensor. The dimensions of the outer diameter of the cap, D_{co} and the height of the cap, h_c are mainly determined by the technology of mounting the cap on the shaft. They have little effect on the sensor performance at high frequencies as the induced eddy current in the cap flows less in the cap edge

Reducing the gap g_t (shown in Fig. 4) between the shield and the rotating shaft could increase the sensor voltage because of increased flux linkage. Fig. 20 shows a modified model of coils with decreased coils height, h_w from 2.5 mm to 1.25 mm and increased coils thickness, t_w from 2 mm to 4 mm, while the magnetic gap between coils and rotating part, $g_m = 2$ mm, the coil area, and the number of turns remained the same. g_t is therefore reduced from 8 mm to 5.5 mm. 3D FEM calculations show that the sensor voltage could increase by 29 % for an iron shaft only and by 38% for an iron shaft with an aluminum cap in the

The final version of his paper was published at Sensors and Actuators 365 (2024), 114917, <https://doi.org/10.1016/j.sna.2023.114917>

configuration shown in Fig. 20. Therefore, the sensitivity of the sensor considerably improves in the modified model. The accuracy of the sensor would be improved as the modified model shows higher sensitivity.

Fig. 21 presents the voltage versus magnetic gap, g_m , for the modified model in Fig. 20. The sensor voltage decreases more in the modified model in Fig. 21 a) in comparison with the voltage in the original model in Fig. 6 a). This is caused by a shorter g_t and, therefore, a bigger g_m/g_t ratio in the modified model. Using a nonmagnetic cap would compensate the effect of higher susceptibility of the modified model of the sensor to magnetic gap g_m change, as shown in Fig. 21 b) for an aluminum cap with a thickness of 0.5 mm.

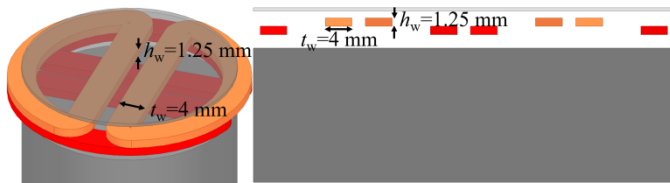


Fig. 20. Modified model of coils with increased coils thickness t_w and reduced coils height h_w

TABLE IX

CALCULATED VOLTAGE TO CURRENT RATIO, IRON SHAFT + CAP – 3D FEM

U_p / I , mV/A ($I = 10$ mA)		Al	Copper
Iron-a + cap – $\mu_r = 100$ 3000 rpm, 1000 Hz	$t_c = 1.0$ mm	638	487
	$t_c = 0.50$ mm	768	635
	$t_c = 0.25$ mm	625	808

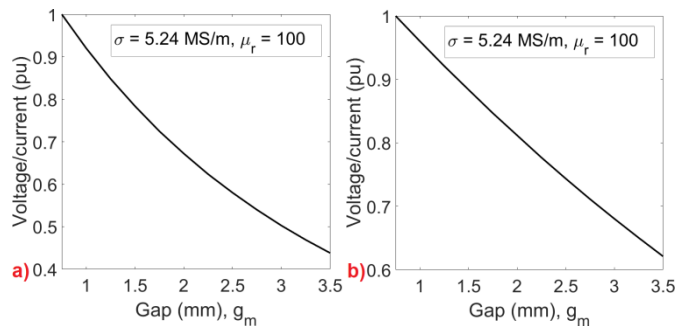


Fig. 21. The voltage to current ratio versus the magnetic gap, g_m , for the modified mode in Fig. 20 using 2D FEM, a) only iron shaft, b) iron shaft with aluminum cap with thickness 0.5 mm -1000 Hz and 3000 rpm

The number of turns in each coil can be increased above 500 to enhance the sensor voltage with the same current in the excitation coil. A higher number of turns occupies a larger space, which causes larger sensor with a bigger gap between the magnetic shield and the rotating part, g_t and a larger inductance and reactance of the excitation coils. In contrast, a bigger g_t causes lower sensitivity, and a higher source voltage is required for the larger inductance and reactance of the excitation coils to maintain the same excitation coils current.

VI. DISCUSSION

Fig. 22 shows the model of the proposed eddy current speed sensor when it works: a) with only an excitation coil and two pick-up coils and b) with only one pick-up coil and two excitation

coils. The values of the real and imaginary components of the sensor voltage become exactly half for the condition of Fig. 22 in comparison with the sensor operating with two excitation and pick-up coils. This is an advantage for the sensor in terms of appropriate fault tolerant capability when the excitation coils and the pick-up coils are connected in parallel.

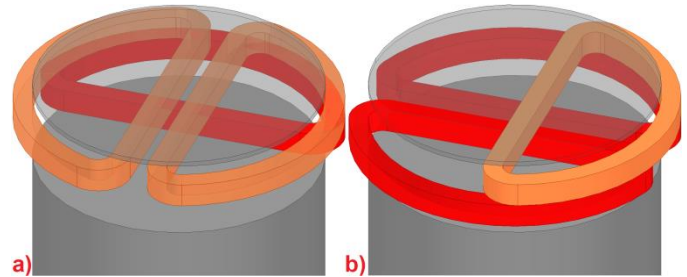


Fig. 22. Model of eddy current speed sensor when it operates a) with only one excitation coil and b) with only one pick up coil

The temperature of the shaft changes the value of σ and μ_r . The material properties of the iron shaft, σ and μ_r , change the sensitivity of the sensor. Temperature compensation is therefore required to stabilize the performance of the sensor at the working temperatures of the shaft. Using a nonmagnetic cap minimizes the effect of the material properties of the shaft on the performance of the sensor. Changes in the magnetic gap between the coils and the shaft affect the sensitivity of the sensor; this influence is smaller for larger gap values. Each of the real and imaginary components of the voltage can be used for a speed meter, as both components show high linearity versus speed. Therefore, one component can be used for temperature or gap deviation compensation while the other component is used for speed measurement. Simultaneous excitation by 2 to 3 frequencies can be used for compensation, as the voltage at one frequency can be utilized for speed measurements and the voltages at other frequencies can be utilized for compensation purposes.

The nonlinearity error of the speed sensor proposed in this paper can be as low as 0.15%, which shows the high accuracy of the sensor for the rotating speed measurement. It is lower than the reported 1.0% nonlinearity error in a commercial magnetic speed sensor with a contact configuration based on a tachometer and a no-contact configuration based on infrared [42]. The achievable resolution for the proposed eddy current speed sensor is 0.25 rpm using an SR830 DSP lock-in amplifier with a 16-bit Analog-to-Digital Converter.

Fig. 23 a) shows an applied speed step from 1000 rpm to 3000 rpm with a time rise of 0.125 ms, as shown in Fig. 23 a) in a 2D FEM model at 1000 Hz and 4000 Hz. The voltage to current ratio is calculated for a solid iron shaft. The sensor voltage shows steady state results in less than 1 ms; therefore, the rotating speed measurement in high dynamic conditions can be accurately achieved. A shorter transient part in the sensor voltage is more feasible at higher frequency, 4000 Hz in comparison with 1000 Hz.

The final version of his paper was published at
Sensors and Actuators 365 (2024), 114917, <https://doi.org/10.1016/j.sna.2023.114917>

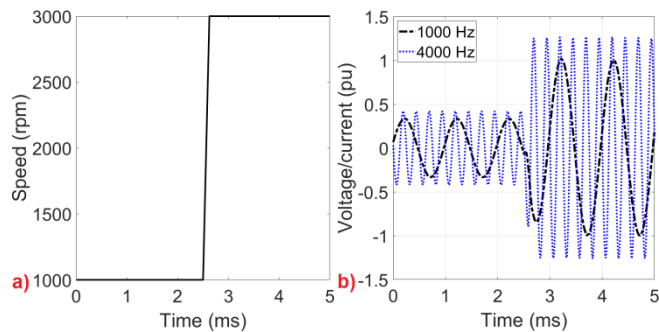


Fig. 23. a) speed step, b) the voltage-to-current ratio versus time at 1000 Hz and 3000 Hz (2D FEM)

A schematic view of installed eddy current speed sensors on the non-drive end of shafts of axial induction machines is shown in Fig. 24 as potential practical applications. Axial flux electrical machines are built to accommodate a propulsion system in a room with a limited axial length. Therefore, the proposed speed sensor with a short axial length is well suited for the control and maintenance of axially compact electrical and mechanical machines. The application of the proposed axial flux eddy current speed sensor is general for all types of rotating machinery with conductive, nonmagnetic, and magnetic iron and steel shafts.

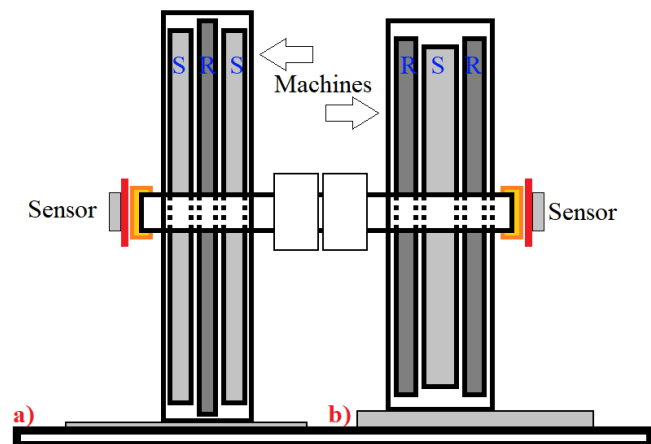


Fig. 24. A schematic model of eddy current speed sensor mounted on the non-drive end of shafts for axial flux induction machines a) as a prime mover (motor) or b) as a load (generator)

VII. CONCLUSION

An axial flux eddy current sensor with a novel configuration of the coils has been presented for speed measurements of the rotating shaft. The speed sensor shows a nonlinearity error of only 0.15% compared to 0.5 % for the previous design [37]. The perpendicular arrangement of the excitation and pick-up coils improves the sensitivity of the sensor. The sensor is compact, with a total axial length of 6.5 mm. The sensitivity of the sensor can be increased substantially by optimizing the nonmagnetic caps and the dimensions of the coils. The utilization of a nonmagnetic cap also reduces the susceptibility of the sensor to the material properties of the iron shaft and to the changes of the airgap between the sensor and the shaft. The proposed eddy current sensor shows high fault tolerant capability when one of

the two excitation coils or pick-up coils connected in parallel is disconnected.

2D and 3D FEM have been used for performance analyses and evaluations of the axial flux eddy current sensor. Optimization of the sensor was performed using FEM to enhance the sensitivity of the sensor.

REFERENCES

- [1] Z. Xiao, Q. Wang, P. Sun, B. You, and X. Feng, "Modeling and energy-optimal control for high-speed trains," *IEEE Trans. Transportation Electrification*, vol. 6, no. 2, pp. 797-807, June 2020
- [2] E. Libbos, E. Krause, A. Banerjee, and P. T. Krein, "Winding layout considerations for variable-pole induction motors in electric vehicles," *IEEE Trans. Transportation Electrification*, Early access (2023)
- [3] T. Gundogdu, Z. Q. Zhu, and J. C. Mipo, "Optimization and improvement of advanced nonoverlapping induction machines for EVs/HEVs," *IEEE Access*, vol. 10, pp.13329-13353, 2022
- [4] E. Libbos, E. Krause, A. Banerjee, and P. T. Krein, "Inverter design considerations for variable-pole induction machines in electric vehicles," *IEEE Trans. Power Electronics*, vol. 37, no. 11, pp. 13554-13565, Nov. 2022
- [5] Y. Okade, et al, REBCO trapezoidal armature windings for superconducting induction motors, *IEEE Trans. Applied Superconductivity*, vol. 32, no. 6, 5201706, Sept. 2022
- [6] N. Zhao and N. Schofield, "An induction machine design with parameter optimization for a 120-kW electric vehicle," *IEEE Trans. Transportation Electrification*, vol. 6, no. 2, pp. 592-601, June 2020
- [7] J. Mei, C. H. T. Lee, and J. L. Kirtley, "Design of axial flux induction motor with reduced back iron for electric vehicles," *IEEE Trans. Vehicular Technology*, vol. 69, no. 1, pp. 293 - 301, Jan. 2020
- [8] Z. Cao, A. Mahmoudi, S. Kahourzade, W. L. Soong, "An overview of axial-flux induction machine," *2021 31st Australasian Universities Power Engineering Conference (AUPEC)*, 26-30 September 2021, Perth, Australia
- [9] S. Kahourzade, A. Mahmoudi, E. Roshandel, and Z. Cao, "Optimal design of Axial-Flux Induction Motors based on an improved analytical model," *Energy*, vol. 237, 121552, 15 Dec. 2021
- [10] J. Mei, Y. Zuo, C. H. T. Lee, and J. L. Kirtley, "Modeling and optimizing method for axial flux induction motor of electric vehicles," *IEEE Trans. Vehicular Technology*, vol. 69, no. 11, pp. 12822 - 12831, Nov. 2020
- [11] X. Yan, and Ming Cheng, "An MRAS observer-based speed sensorless control method for dual-cage rotor brushless doubly fed induction generator," *IEEE Trans. Power Electronics*, vol. 37, no. 10, pp. 12705-12714, Oct. 2022
- [12] Yun Zuo, et al, "An adaptive active disturbance rejection control strategy for speed-sensorless induction motor drives," *IEEE Trans. Transportation Electrification*, vol. 8, no. 3, pp. 3336-3348, Sept. 2022
- [13] Y. Wang, W. Hua, C. Zhang, Z. Wu, and H. Zhang, "Concept and implementation of embedded magnetic encoder in flux-switching permanent-magnet machines," *IEEE Trans. Industrial Electronics*, vol. 69, no. 11, pp. 11796-11806, Nov. 2022
- [14] C. G. Dias and L. C. da Silva, "Induction motor speed estimation based on airgap flux measurement using Hilbert transform and fast Fourier transform," *IEEE Sensors J.*, vol. 22, no. 13, pp. 12690-12699, July 2022
- [15] X. Guo, Y. Wang, X. Chen, Z. Chen, W. Hua, and R. Zhong, "An embedded magnetic encoder based rotor position estimation for switched reluctance machine," *IEEE Trans. Transport. Electrification*, 2023 (Early Access)
- [16] S. A. X. Gao, C. Lu, D. Yao, M. Lu, M. Zhang, Y. Sun, H. Fang, and D. Li, "Self-powered flexible sensor based on Triboelectric nanogenerators for noncontact motion sensing," *IEEE Sensors J.*, vol. 22, no. 13, pp. 12547- 12559, July 2022
- [17] C. E. Robinson, "Analog tachometers," *IEEE Trans. Industry & General Applications*, vol. IGA-2, no. 2, pp. 144-146, March/April 1966
- [18] Z. Shi, et al, "Design and development of a tachometer using magnetoelectric composite as magnetic field sensor," *IEEE Trans. Mag.*, vol. 54, no. 7, 4000604, July 2018
- [19] Y. Vazquez-Gutierrez, D. L. O'Sullivan, and R. C. Kavanagh, "Small-signal modeling of the incremental optical encoder for motor control,"

The final version of his paper was published at
Sensors and Actuators 365 (2024), 114917, <https://doi.org/10.1016/j.sna.2023.114917>

- IEEE Trans. Industrial Electronics*, vol. 67, no. 5, pp. 3452-3461, May 2020
- [20] S. A. Seyed-Bouzari, H. Saneie, Z. Nasiri-Gheidari, "Analysis and compensation of the longitudinal end-effect in variable reluctance linear resolvers using magnetic equivalent circuit model," *IEEE Trans. Transportation Electrification*, Early Access (2023)
- [21] X. Ran, J. Shang, M. Zhao, and Z. Yi, "Improved configuration proposal for axial reluctance resolver using 3-D magnetic equivalent circuit model and winding function approach," *IEEE Trans. Transportation Electrification*, vol. 9, no. 1, pp. 311-321, March 2023
- [22] C. Gong, S. Li, T. Habetler, J. A. Restrepo, and B. Soderholm, "Direct position control for ultrahigh-speed switched-reluctance machines based on low-cost nonintrusive reflective sensors," *IEEE Trans. Ind. Appl.*, vol. 55, no. 1, pp. 480-489, Jan.-Feb. 2019
- [23] A. M. Mahfouz, M. H. Mohammed, S. Shams, and H. S. Abbas, "Accurate and simple modeling of eddy current braking torque: analysis and experimental validation," *IEEE Trans. Magnetics*, vol. 59, no. 4, 800209, April 2023
- [24] J. Li, Y. Li, J. Xu, J. Luo, S. Xu, Y. Li, M. Zeng, H. Yu, L. Cui, X. Song, and G. Ma, "Calculation and characterization of braking performance for rail eddy current brake with AC excited ring-winding armature," *IEEE Trans. Industry Applications*, vol. 59, no. 2, pp. 1614-1625, March/April 2023
- [25] J. A. Shercliff, *The Theory of Electromagnetic Flow Measurement*, Cambridge, U.K.:Cambridge Univ. Press, 1962
- [26] H. Yang, G. Qing, Y. Chen, and H. Zhao, "Optimization of coil width and magnetic field switching speed for non-contacted electromagnetic flowmeter," *IEEE Sensors J.*, vol. 20, no. 10, pp. 5329-5335, May 2020
- [27] C. C. Feng, W. E. Deeds and C. V. Dodd, "Analysis of eddy-current flowmeters", *J. Appl. Phys.*, vol. 46, no. 7, pp. 2935-2940, 1975
- [28] A. Onat and S. Markon, "Theoretical and experimental analysis of eddy current contactless speed sensors for linear motor elevators," *IEEE Sensors J.*, vol. 22, no. 7, pp. 6345-6352, April 2022
- [29] N. Takehira, A. Tanaka, K. Toda, "Analysis of a speed-meter utilizing eddy current effect," *The Trans. Inst. Elect. Eng. Japan A*, vol. 97, no. 9, pp. 457-464, Sept. 1977
- [30] N. Takehira and A. Tanaka, "Analysis of a perpendicular-type eddy-current speed meter", *IEE Proc. A Phys. Sci. Meas. Instrum. Manage. Edu. Rev.*, vol. 135, no. 2, pp. 89-94, Feb. 1988
- [31] T. Itaya, K. Ishida, A. Tanaka, and N. Takehira, "Exact analysis of a linear velocity sensor," *IEEE Trans. Inst. & Meas.*, vol. 70, 6002106, 2021
- [32] T. Sonoda, R. Ueda, K. Fujitani, T. Irida and S. Tatata, "DC magnetic field type eddy current speed sensor detecting cross magnetization field with amorphous core", *IEEE Trans. Magn.*, vol. 21, no. 5, pp. 1732-1734, Sep. 1985
- [33] E. Cardelli, A. Faba and F. Tissi, "Contact-less speed probe based on eddy currents", *IEEE Trans. Magn.*, vol. 49, no. 7, pp. 3897-3900, Jul. 2013
- [34] B. Feng, K. Deng, L. Xie, S. Xie, and Y. Kang, "Speed measurement method for moving conductors based on motion-induced eddy current," *IEEE Trans. Inst. & Meas.*, vol. 72, 6005608, 2023
- [35] M. Mirzaei and P. Ripka, "A linear eddy current speed sensor with a perpendicular coils configuration," *IEEE Trans. Vehicular Technology*, vol. 70, no. 4, pp. 3197 - 3207, April 2021
- [36] M. Mirzaei, P. Ripka, V. Grim, and A. Chirtsov, "Design and optimization of an eddy current speed sensor for rotating rods," *IEEE Sens. J.*, vol. 20, no. 20, pp. 12241-12251, June 2020
- [37] M. Mirzaei, P. Ripka, and V. Grim, "An axial airgap eddy current speed sensor," *IEEE Trans. Ind. Elect.*, vol. 69, no. 9, pp. 9586-9595, Sept. 2022
- [38] M. Mirzaei, P. Ripka, and V. Grim, "A novel structure of an eddy current sensor for speed measurement of rotating shafts," *IEEE Trans. Energy Conversion*, vol. 38, no. 1, pp. 170 - 179, March 2023
- [39] D. Rodger, "Modeling movement in electrical machines", *IEEE Trans. Magn.*, vol. 57, no. 6, Jun. 2021.
- [40] C. Hong, W. Huang, and Z. Hu, "Design and analysis of a high-speed dual stator slotted solid-rotor axial-flux induction motor," *IEEE Trans. Transportation Electrification*, vol. 5, no. 1, pp. 71-79, March 2019
- [41] Y. Du, Y. Huang, B. Guo, F. Peng, and J. Dong, "Semianalytical model of multiphase Halbach array axial flux permanent-magnet motor considering magnetic saturation," *IEEE Trans. Transportation Electrification*, vol. 9, no. 2, pp. 2891-2901, June 2023
- [42] Digital Tachometer/Sensors and Peripherals, , HT-5510, Digital handheld speedmeter, https://www.onosokki.co.jp/English/hp_e/whats_new/Catalog/PDF/digital_tachometers_2.pdf, Accessed online on 02.08.2023.